

# A shell-based magnetic field model for magnetic proximity detection systems

Jingcheng Li\*, Jacob Carr, Christopher Jobes

The National Institute for Occupational Safety and Health, 626 Cochran's Mill Road, Pittsburgh, PA 15236, USA

## A B S T R A C T

Several magnetic proximity detection systems have been developed for mining vehicles and mobile machinery to protect nearby workers. Magnetic field generators are often used in these systems to establish magnetic fields around the equipment. A sensor worn by a worker provides a measurement of the magnetic flux density that is used to estimate the proximity to the machine. The proximity detection systems currently available for underground mining equipment are capable of identifying whether a worker is near the machine. However, it is a challenge for these systems to accurately locate the worker. Mining machines, which have fast-moving, articulated parts, present hazards that change depending on the situation at hand as well as the specific location of the worker. In addition, the dynamic nature and confined spaces of the mining environment often demand that the workers be close to the machinery. Therefore, in many cases, simply knowing the proximity of a worker may be inadequate. To provide the most effective protection, it would be advantageous to know the worker's exact location relative to specific parts of the machine. To lay the foundation for measuring such a location, we have developed a shell-based model of the magnetic flux density distribution for a ferrite-cored generator. This paper will present an analysis of the model along with a model construction process. Also presented are the laboratory test results of a prototype system that implements this model to determine the exact location of a magnetic sensor using the fields from two generators.

## 1. Introduction

The current research of the National Institute for Occupational Safety and Health (NIOSH) in the field of proximity detection for underground mining equipment has primarily focused on developing the technologies and methodologies to allow magnetic proximity detection systems to determine an exact location of a worker around mobile mining machinery (Carr et al., 2010). This work is motivated by a desire to protect against striking and pinning hazards. Being inspired by the time-of-flight triangulation techniques used in the Global Positioning System (GPS), NIOSH researchers developed a similar means to accurately locate a mine worker as being at the intersection point of two or more magnetic shells from generators mounted on a machine. A magnetic shell is defined to contain all points of equal magnetic flux density around a magnetic field generator.

Li et al. (2010) introduces an empirical shell-based magnetic flux density distribution model, which describes the shape of a shell. This paper presents a detailed discussion of that model. A model construction process using measured data is also presented. NIOSH has successfully implemented an application of the model,

determining the location of a worker as the intersection of multiple magnetic shells. This experimental application of the model will be briefly introduced along with the test results.

## 2. Background

### 2.1. Mining machine hazards

Despite continual safety improvements, the mining industry remains one of the most hazardous working environments, especially for those working in close proximity to mining machinery. It is not uncommon to find workers routinely located within 1–2 m of moving machinery in underground coal mines. Workers have to work in close proximity to mining machinery because of space constraints, extensive operator blind spots, poor visibility and high noise levels. Unexpected machine movement caused by unintentional or incorrect control activation can threaten the safety of workers. Continuous mining machines (CMMs) such as the one shown in Fig. 1 are one of the machines most commonly involved in accidents. Under pressure to maximize production, workers may inadvertently work in dangerous areas around a CMM up to 80% of the time (Buchsbau, 2011).

According to the Mine Safety and Health Administration (MSHA), during the period of 1999–2006 in the United States, there were, on average, 254 accidents per year during routine mining

\* Corresponding author. Tel.: +1 412 386 4751; fax: +1 412 386 6710.

E-mail addresses: jingcheng.li@cdc.hhs.gov (J. Li), jacob.carr@cdc.hhs.gov (J. Carr), christopher.jobes@cdc.hhs.gov (C. Jobes).



Fig. 1. A continuous mining machine at the NIOSH laboratory in Pittsburgh.

and maintenance activities involving remote-control CMMs. MSHA also reports that since 1984, there have been 34 fatalities in which a person was struck or pinned by a CMM. Fig. 2 shows the fatality distribution around a CMM (Dransite et al., 2011). In the figure, numbers indicate the sequence of these accidents; the “X” indicates the general location of the fatality relative to the CMM; the circled numbers indicate that the victim was operating the machine; the square around numbers indicate that the victim was not operating the machine; grey background indicates that the accident occurred while performing maintenance; and white background indicates that the accident happened while either tramming or operating the machine (Dransite et al., 2011).

2.1.1. Need for proximity detection systems

In 2002, MSHA conducted a review of fatal accidents associated with remote-control continuous mining machines and concluded that proximity detection systems could have prevented a substantial number of these accidents. MSHA has since investigated several proximity detection technologies including ultrasonic, radar, infrared and electromagnetic systems. Of these technologies, electromagnetic proximity detection was determined to offer the greatest promise for deployment in the mining environment (Chirdon, 2009).

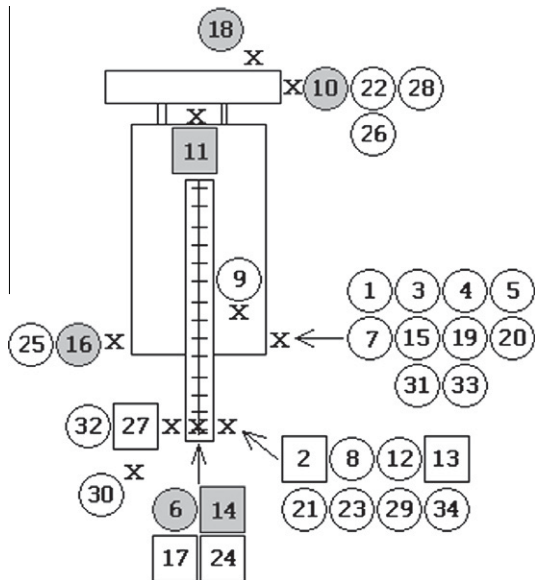


Fig. 2. Locations of remote-control CMM fatal accidents (from Dransite et al. (2011)).

2.2. Proximity detection systems for mining machines

There are currently three electromagnetic proximity detection systems available in the United States, which are undergoing extensive testing in a variety of underground production environments, both domestically and internationally.

2.2.1. Operation principle of magnetic proximity detection systems

Fig. 3 shows the basic components used in these systems. A sinusoidal or modulated current at a carrier frequency between 10 and 100 kilohertz (kHz) flows through a generator consisting of a wire coil wound around a ferrite core to establish a magnetic field. A magnetic sensor worn by a worker detects the magnetic signal and measures the magnetic flux density on three orthogonal axes. These readings are used to calculate the total magnitude of the magnetic flux density ( $B$ ) which is then used to estimate the distance from the machine. This type of proximity detection technology was originally developed at NIOSH (Schiffbauer, 2002).

An essential capability of these systems is to identify whether a person is located within pre-defined zones around a machine. Fig. 4 shows an example of the type of zones typically used for a CMM. In the figure, the inner red area around the CMM is the stop zone, and the outer yellow area is the warning zone. The proximity system should immediately issue a warning if it detects a worker in the warning zone, and stop machine movement if the worker moves into the stop zone. The desired shapes of these zones are often complex and vary depending on the preferences of mine operators who want to allow mine workers to position themselves where they can most effectively and safely perform their jobs (Bartels et al., 2005, 2008). As workers are generally in very close proximity to the machines in confined entryways, high location accuracy is crucial to providing protection to the workers while minimizing the occurrence of nuisance alarms. The safety value of a proximity system may be lost if an acceptable accuracy is not consistently maintained.

To provide sufficient coverage on a large machine like a CMM, a proximity detection system typically includes several generators that, in some systems, are continuously energized and, in other systems, are sequentially or randomly pulsed. With multiple generators, these systems are capable of generating combined magnetic fields to cover the entire space around many types of the mining machinery. It proves to be, however, a difficult challenge to tune the magnetic flux density distributions to match the desired zone shapes like those shown in Fig. 4.

2.2.2. Tuning method for current proximity detection systems

A popular method used to tune a magnetic proximity system is to position the generators in such a way that a particular magnetic shell surface corresponds to the boundary of a zone. This shell then defines a threshold magnetic flux density that can be used to determine whether a worker is located in the shell and, therefore,

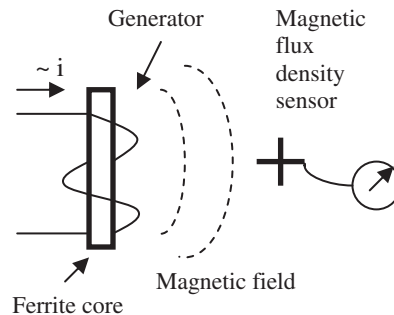


Fig. 3. Main components of a magnetic proximity detection system.

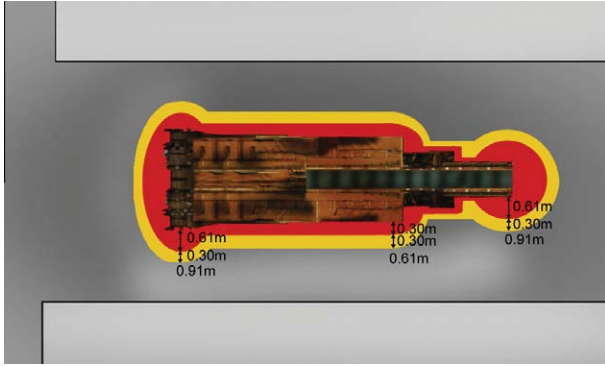


Fig. 4. Zones around a continuous mining machine.

within the corresponding zone. With multiple pulsed generators, logical combinations of such threshold values can define zones of more complex shapes. The accuracy of the zone boundaries defined in this way is typically verified through measurements at a select number of points considered especially hazardous. This approach only provides accurate system calibration under the specific conditions for which the calibration was performed at those limited points. It is not uncommon to find that the magnetic shells selected as the zone boundaries do not match the boundaries of the desired zones over extended areas. Zone identification errors thus become inevitable, resulting in either false alarms or failures to alarm.

If the proximity detection zones are selected to be defined by the electromagnetic shells, the exact shapes and coverage of the zones depend heavily on the configuration of the generators on the machine and other calibration factors. Fig. 5 shows the theoretical zones around a CMM using this method with a four-generator system (Ruff, 2010).

### 2.3. Underlying issue with current proximity detection systems

Mismatch between the magnetic shell surfaces and the desired zone boundaries is primarily caused by tight coupling of two unrelated physical measures, namely the zone boundaries and the magnetic field shapes of the generators. The zone boundaries are defined according to the safety requirements in the human-machine system. The generators, understandably, generate their magnetic fields obeying only the laws of physics. These laws dictate highly nonlinear behavior of the electromagnetic fields, as discussed in later sections. It is highly unlikely that the generated magnetic field distribution patterns will match the desired shapes

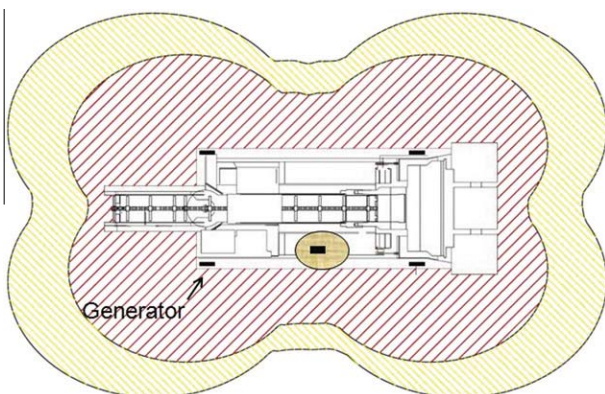


Fig. 5. Theoretical zoning example by choosing a magnetic shell surface as a zone boundary.

of the zone boundaries. This is probably one of the primary reasons that, to this date, there has not been a successful method reported to systematically find a complete geometric match between the magnetic field shells and the zone boundaries around a machine. The issue becomes even more severe in the case of large mobile mining machines, which have irregular shapes, articulating parts, and limited visibility around them. Thus, the current generation of proximity detection systems, which identify a zone using immediate magnetic field flux density measurements could be improved through more accurate sensor location information.

## 3. A radical solution to the issue

NIOSH researchers suggest a novel approach to resolve this issue by decoupling those two unrelated physical measures (the zone boundaries and the magnetic field shapes) and coupling the systems with only two related physical measures, the sensor location on two coordinate systems. In this approach, the zones are defined on a coordinate system fixed to the machine, and the magnetic field of each generator is defined on a coordinate system fixed to the generator. Although these coordinate systems are independent, they share the same measurement units and can be associated with each other. By coupling these two coordinate systems, a point on one coordinate system can be systematically and uniquely mapped to the corresponding point on another coordinate system. This implies that if the location of a magnetic sensor is completely determined on the magnetic field coordinate system, its corresponding location on the machine coordinate system can be unambiguously determined through a point mapping process. The basic idea for this approach is to use  $B$  readings from multiple generators to determine the exact location of the sensor on the magnetic field coordinate system and then map it to the machine coordinate system to determine its exact location and the zone in which it lies.

### 3.1. Solution methodology

This approach requires a three-step procedure. The first step is to define a shell-based magnetic distribution model for an individual generator in its own coordinate system and a common coordinate system for all generators in the system. The next step is to generate the magnetic shells using the  $B$  readings from the fields of these generators and locate the intersection point of these shells on the common coordinate system. The final step is to map the intersection location onto the machine coordinate system to determine the sensor's location relative to a specific part of the machine, and the zone in which the sensor lies.

### 3.2. Solution advantages

This approach eliminates the need to geometrically match the boundaries of the zones and the magnetic field shell surfaces. This allows the implementation of practically any zone shape and should greatly reduce rates of nuisance alarms and failures to alarm. In addition, this technique allows for dynamic definition of zones for different areas around the machine or during different tasks, which may provide for more versatility and more effectiveness in protecting workers. For example, the stop zone could be substantially narrowed on the sides of the machine to allow a worker to stand closer during a cutting operation because there should be a lesser chance that the machine could hit him in this operation. Clearly, a magnetic field distribution model for an individual generator forms the foundation for this approach.

## 4. The shell-based magnetic field distribution model

### 4.1. Three-dimensional magnetic field distribution model

The general properties and parameters of the shell-based magnetic flux density distribution model for a generator are as follows. Eq. (1) shows the model covering the three-dimensional (3-D) space around a magnetic generator. The model defines a magnetic shell with a given  $B$  value. The coordinate system and the symbols used in Eq. (1) are defined as shown in Fig. 6 in which a generator of length  $L$  lies along the  $x$ -axis and is centered at the origin. Eqs. (1a) and (1b) are equivalent representations of the shell functions in the Cartesian and the direction cosine systems, respectively. In Eq. (1),  $\rho$  represents the distance from a point on the shell to the origin;  $\alpha$ ,  $\beta$ , and  $\gamma$  represent the angles from the  $x$ -,  $y$ -, and  $z$ -axes, respectively, to the line on which  $\rho$  is measured. A shell can be generated from Eq. (1) with a given  $B$  reading, and each shell is described by a function in the form of either Eqs. (1a) or (1b) that is uniquely and completely defined by two parameters,  $a$  and  $b$ , as defined in terms of the  $B$  reading by Eqs. (1c) and (1d). The shell shape parameter,  $a$ , determines the variation of the shell from its basic shape of a sphere with radius,  $b$ , the shell size parameter. Fig. 7 shows plots of three magnetic shells generated from measured data to illustrate the shape variation that this model is designed to capture. The functions for these three shells in a direct cosine system are included in Eq. (2). The uniform accuracy of Eq. (1) has been shown for the space beyond half of the generator length, or  $L/2$ , but has not been tested within the range of  $a + b < L/2$ .

$$\text{Shell}(x,y,z|B) \text{ or } \text{Shell}(\rho, \alpha, \beta, \gamma|B) = \begin{cases} (x^2 + y^2 + z^2)^{1/2} = a \left( \frac{x^2 - y^2 - z^2}{x^2 + y^2 + z^2} \right) + b & (1a) \\ \text{or } \rho = a(\cos^2 \alpha - \cos^2 \beta - \cos^2 \gamma) + b & (1b) \\ \text{for } a + b > L/2, 0 \leq \alpha, \beta, \gamma < \pi & (1c) \\ a = c_a B^{-d_a} & (1d) \\ b = c_b B^{-d_b} & (1d) \\ \text{for } B > 0 & (1) \end{cases}$$

$$\begin{cases} \text{Inner shell :} \\ \rho = 91.6(\cos^2 \alpha - \cos^2 \beta - \cos^2 \gamma) + 100.5 \text{ (mm)} \\ \text{Shell between inner and outer :} \\ \rho = 63.7(\cos^2 \alpha - \cos^2 \beta - \cos^2 \gamma) + 321.0 \text{ (mm)} \\ \text{Outer shell :} \\ \rho = 86.9(\cos^2 \alpha - \cos^2 \beta - \cos^2 \gamma) + 670.5 \text{ (mm)} \\ 0 \leq \alpha, \beta, \gamma < \pi \end{cases} \quad (2)$$

The shell shape function (1c) has two positive constants,  $c_a$ , the shell base shape constant, and,  $d_a$ , the shell shape changing constant. Similarly, the shell size function (1d) has two positive

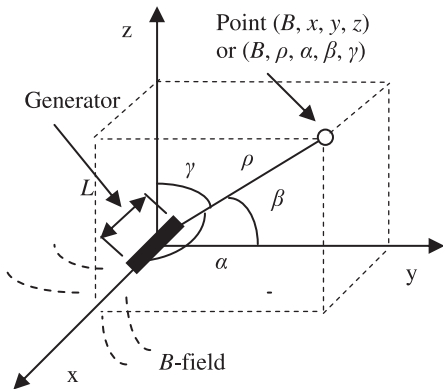


Fig. 6. Generator and its magnetic field coordinate systems.

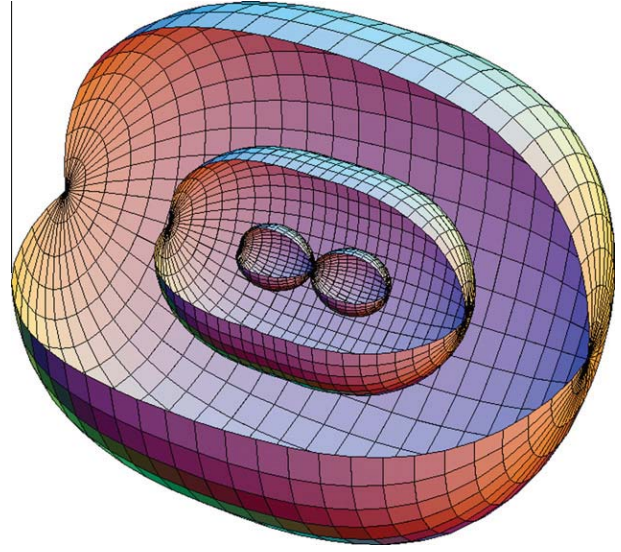


Fig. 7. Illustration of magnetic shells around a magnetic generator.

constants,  $c_b$ , the shell base size constant, and,  $d_b$ , the shell size changing constant. These four constants have fixed values for a given steady magnetic field and completely describe the magnetic field in its defined space. These constants are defined by the physical distribution characteristics of a given magnetic field that are determined by many factors: primarily the length of the ferrite core, permeability of the core material and medium, the number of turns of the coil, the current flowing through the coil and the impedance of the generator. These constants can also be determined empirically using data from magnetic field measurements.

The ratio of  $a-b$  is called the shell shape changing ratio, and it is a good indicator of the variation of the shell shape from spherical. Its value is uniquely determined by the value of  $B$ , as shown in Eq. (3). No two shells have the same shell shape changing ratio, and, therefore, no two shells have the same shape. It has been observed that, typically  $0 < c_a < c_b$  and  $0 < d_a < d_b$ , and that as the value of  $B$  increases, the ratio  $a/b$  will also increase. As  $B$  is larger close to the generator, the ratio  $a/b$  increases close to the generator, resulting in greater deviation from a spherical shape to a more deeply concaved shell. Conversely, further from the generator, the value of  $B$  is smaller yielding a ratio  $a/b$  that is smaller, and the resulting shell will be more spherical in shape. Fig. 7 illustrates this variation in shape and size.

$$\frac{a}{b} = \frac{c_a B^{-d_a}}{c_b B^{-d_b}} = \frac{c_a}{c_b} B^{d_b - d_a} \quad (3)$$

#### 4.1.1. Discussion of the model

With a single  $B$  reading it is only possible to determine the shell on which the measurement is made. The exact distance between the sensor and the generator cannot be directly determined since the shell is never a perfect sphere and points at different locations on the shell will have different distances to the generator.

#### 4.2. Two-dimensional magnetic field model

In certain cases, it may be sufficient to assume that the generators and the workers are located in a two-dimensional (2-D) plane. In this case, the model in Eq. (1) can be simplified to its 2-D form by letting  $z = 0$  or  $\gamma = 90^\circ$  as given in Eq. (4). The coordinate systems and symbols used in Eq. (4) are defined as shown in Fig. 8. Eqs. (4c) and (4d) are the same as Eqs. (1c) and (1d).

Similar to obtaining a 3-D shell, a 2-D shell can be obtained from a single  $B$  measurement, in which the shell shape parameter,  $a$ , and the shell size parameter,  $b$ , can be obtained from Eqs. (4c) and (4d). The constants,  $c_a$ ,  $d_a$ ,  $c_b$  and  $d_b$ , in the shell shape function (4c) and the shell size function (4d) are the same as those in functions (1c) and (1d).

$$\text{Shell}(x, y|B) \text{ or } \text{Shell}(\rho, \alpha|B) = \begin{cases} (x^2 + y^2)^{1/2} = a \left( \frac{x^2 - y^2}{x^2 + y^2} \right) + b & (4a) \\ \text{or } \rho = a(\cos 2\alpha) + b & (4b) \\ \text{for } a + b > L/2, |\alpha| \leq 2\pi & \\ a = c_a B^{-d_a} & (4c) \\ b = c_b B^{-d_b} & (4d) \\ \text{for } B > 0 & (4) \end{cases}$$

### 4.3. Alternative shell-based models

Some other empirical models define the shells simply as geometrical shapes such as ellipsoids and spheres. These models were also evaluated with laboratory measurement data during the course of this research. The evaluation showed that, among these models, the models given in Eqs. (1) and (4) produced the smallest statistical errors over a wide range of space around the generator.

## 5. A method for magnetic field measurement data collection

### 5.1. Data types

Before the model can be used to define shells for a particular generator, the model has to be constructed for that generator using measured magnetic flux density data.

The researchers conducted experiments at the NIOSH laboratory in Pittsburgh, and collected data to construct, verify, and check the accuracy of the model.

In these experiments, magnetic flux density magnitude data were collected at known locations throughout the space around a generator. The data contain two parts, the  $B$  readings and the locations of the sensor on the coordinate system of the generator.

### 5.2. Experiment setup for data collection

The experiment setup included two parts, the instrumentation and the positioning measurement setup. The instrumentation was used to provide an AC current flow to the generator to produce a steady magnetic field. The positioning measurement setup consisted of a platform on which a magnetic flux density,  $B$ , could be read, and the orientation and location of a magnetic probe or sensor could be measured at selected points.

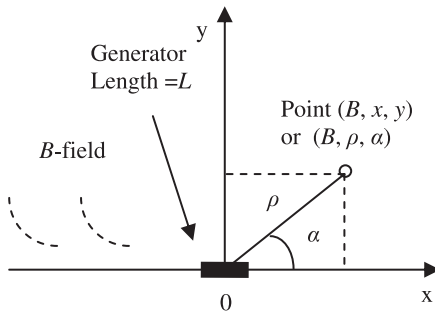


Fig. 8. Generator and its 2-D magnetic field coordinate systems.

### 5.2.1. Instrumentation setup

The basic instrumentation is shown in Fig. 9. An HP 33120A function generator provided a continuous sinusoidal signal that was fed into both an oscilloscope for signal monitoring and an amplifier. Experiments were conducted with both 10 kHz and 75 kHz signals. A Tektronix TDS 30320 and an Agilent DS090254A oscilloscope were used to monitor the input signal voltage and its waveform as well as the current flowing through the generator. A Sony XM-2100GTX amplifier was used to amplify the 10 kHz signal and a Krohn-Hite Model 7500 amplifier to amplify the 75 kHz signal.

Two types of generators were constructed: one using an MN60-2573-970-07 (permeability of 6500 H/m) 25.4 mm × 25.4 mm × 304.8 mm square-cross-section core from Ceramic Magnetics, Inc. and the other using an RX-1000-7500S-M25 (permeability of 2500 H/m) 190.5 mm × 25.4 mm diameter cylinder core from National Magnetics Group. Both cores belong to the Mn-Zn ceramic ferrite family. Various numbers of coil turns were tested for each of these cores. A BCP-522 current probe was used to monitor the magnitudes of the currents flowing through the generator. The current magnitude readings were monitored on the oscilloscope. An IDR-200 Gauss meter was used to measure magnitude of the vector sum magnetic flux density,  $B$ , around the generator in units of milliGauss (mG).

### 5.2.2. Setup for magnetic field and location measurements

Fig. 10 shows the setup for positioning the Gauss meter on the defined coordinate system. A Cartesian grid and a polar grid were drawn on a piece of paper, which was laid flat on a wooden platform with the generator located along the  $x$ -axis and centered at the origin. The  $y$ -axis was perpendicular to the axis of the generator. A number of radial lines were drawn starting from the origin at a variable angle  $\alpha$ . The angle  $\alpha$  was varied with increments from 2° to up 15° in different experiments.

At each of the measurement locations, the  $B$  reading and the location of the point expressed in either Cartesian ( $x, y$ ) or polar ( $\rho, \alpha$ ) coordinates were recorded. The data were recorded as ( $B, x, y$ ) or ( $B, \rho, \alpha$ ), where  $B$  is in mG, and  $x, y$ , and  $\rho$  are in mm.

In order to cover sufficient space around a generator and to permit a statistical evaluation of the model, many independent sets of measurement data were collected, each at a fixed  $B$ . Each of the data sets contained measurements at between 28 and 150 locations. Each of these data sets corresponded to a magnetic shell. Fig. 11 shows three of these data sets.

### 5.3. Discussion on actual data

The data show that the distance from a point on a given shell to the generator is dependent on where on a shell the point is located.

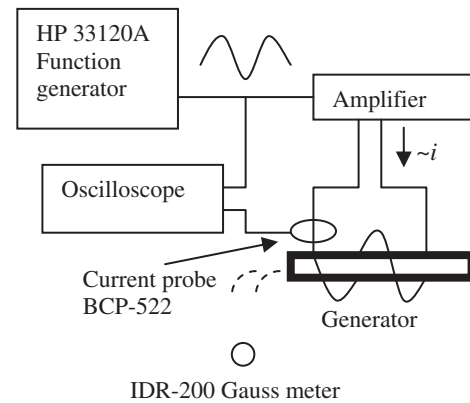


Fig. 9. Instrumentation for magnetic field generation and monitoring.

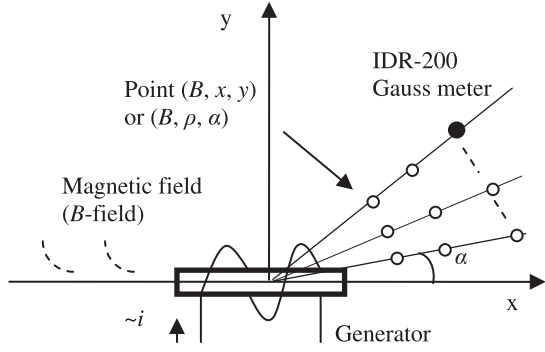


Fig. 10. Setup for 2-D magnetic flux density and location measurements.

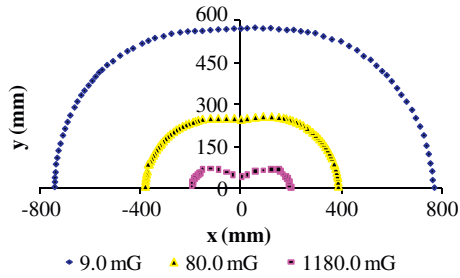


Fig. 11. The magnetic shells from the measurement data.

Therefore, the distance from the measurement point to the generator center cannot be determined with only a single magnetic flux density measurement.

The data also show that the magnetic flux density readings decrease rapidly and nonlinearly with increasing distance from the generator. The readings also decrease at different rates along different directions. The rate of decrease also varies with the length of the ferrite rods.

## 6. Construction of the model

### 6.1. Preparation for model construction

The magnetic field measurements are then used to construct a model specific to the field in which the measurements were taken. Construction of the model refers to the process by which the constants  $c_a$ ,  $d_a$ ,  $c_b$  and  $d_b$  in Eqs. (1) or (4), which completely define that magnetic field, are determined. Because of the rotationally symmetric nature of the fields, constants determined from measurements within a 2-D plane through the field should also apply to the 3-D model. Thus, only the construction process using the 2-D model is discussed in this section.

Due to the highly nonlinear nature of the fields, constructing an accurate model of the magnetic field around a generator requires many sets of measurement data, each containing many measurements at different locations with a fixed  $B$  reading. In the development of the construction process,  $M$  sets of data at different  $B$  readings are taken, forming  $M$  individual shells. Each of the sets contains  $N$  location measurements with the same  $B$  reading.  $(B_j, \rho_{ji}, \alpha_{ji})$  will denote each of the individual measurements, where  $B_j$  is a fixed magnetic flux density reading for data set  $j$ ,  $\rho_{ji}$  is the  $i$ th measured distance for set  $j$ , and  $\alpha_{ji}$  is the  $i$ th measured angle for set  $j$ ,  $i = 1, 2, 3, \dots, N$ , and  $j = 1, 2, 3, \dots, M$ .

There are two steps to complete the construction process. The first step is to produce the shell shape and size parameters  $(a, b)$  for each of the  $M$  individual shells, and the second step is to use all of these shells to determine the values for  $c_a$ ,  $d_a$ ,  $c_b$  and  $d_b$ .

### 6.2. Construction of the shell function

#### 6.2.1. An optimal construction method for the shell function

To construct a shell function from the  $j$ th set of the data involves determining the values of  $a$  and  $b$  in the shell function (4b) from readings at  $N$  2-D locations  $(B_j, \rho_{ji}, \alpha_{ji})$ ,  $i = 1, 2, 3, \dots, N$ .  $S(B_j, a, b)$  designates a single shell where  $B_j$  is the magnetic flux density. Because the location readings are only required in this step, the index  $j$  is not needed and will be dropped in this section.

There are several ways to determine a shell  $S(B, a, b)$ . The preferred method if  $N \gg 3$  is to use a least squares regression to find the optimum values for  $(a, b)$ . In this method, the squared error,  $R$ , defined in Eq. (5), which is derived from Eq. (4b), is minimized by least squares regression. This gives the formulas for the optimum expressions for  $a$  and  $b$  shown in Eq. (6).

$$R = \sum_{i=1}^N [\rho_i - (a \cos(2\alpha_i) + b)]^2 \quad (5)$$

$$\begin{bmatrix} a \\ b \end{bmatrix} = \frac{\begin{bmatrix} N \sum_{i=1}^N \rho_i \cos(2\alpha_i) - \sum_{i=1}^N \rho_i \sum_{i=1}^N \cos(2\alpha_i) \\ \sum_{i=1}^N \rho_i \sum_{i=1}^N \cos^2(2\alpha_i) - \\ - \sum_{i=1}^N \rho_i \cos(2\alpha_i) \sum_{i=1}^N \cos(2\alpha_i) \end{bmatrix}}{N \sum_{i=1}^N \cos^2(2\alpha_i) - \left( \sum_{i=1}^N \cos(2\alpha_i) \right)^2} \quad (6)$$

This method has been extensively used in this work. For example, the shell function shown in Eq. (7) was determined using this method for the data set with  $B = 25.00$  mG in one of the experimental trials. A total of 85 points taken from  $0^\circ$  to  $180^\circ$  on the plane were used to find the values for  $(a, b)$ . The regression shows the mean modeling error is virtually zero; the standard deviation is 6.3 mm; the max error is  $|-12.0|$  mm. Graph A in Fig. 12 shows the plots of both the actual and the generated data from Eq. (7).

$$\rho = 69.04 \cos(2\alpha) + 422.71 \text{ (mm)}, \quad |\alpha| \leq \pi \quad (7)$$

Graph B in Fig. 12 shows similar plots of another set of the data for which the shell function is shown in Eq. (8) with  $B = 170.00$  mG. A total of 54 points taken from  $0^\circ$  to  $180^\circ$  on a plane were used to find the values for  $(a, b)$ . The mean modeling error is virtually zero; the standard deviation is 3.6 mm; the maximum error is  $|-7.0|$  mm. The shell looks like neither a circle nor an ellipse.

$$\rho = 65.03 \cos(2\alpha) + 248.21 \text{ (mm)}, \quad |\alpha| \leq \pi \quad (8)$$

These two examples are representative of all the measurements taken for this work. The values of  $(a, b)$  obtained in this way can be used in the 3-D model shown in Eq. (1). The plots in Fig. 7 were the 3-D models obtained by taking the values of  $(a, b)$  generated using the 2-D measurement data plotted in Fig. 11.

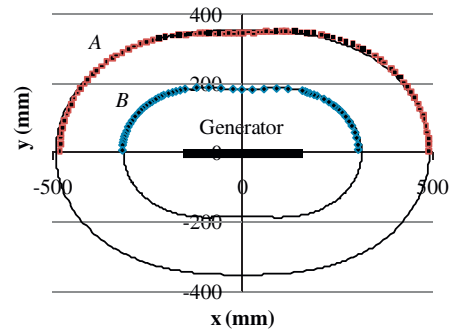


Fig. 12. Plots of the actual data (dotted half shells) and the associated shells generated from the derived model.

### 6.2.2. A simplified construction method for the shell function

While the least squares method provides excellent estimation of the shell parameters, it may not always be practical in a working environment because of time and space constraints. Therefore, an alternative method has been developed to estimate the parameters ( $a, b$ ) from only a few measurements. Referring to Fig. 10, suppose the measurements are made on radii at the angles of  $\alpha = 0^\circ, 30^\circ, 45^\circ, 90^\circ, 135^\circ, 150^\circ$  and at the corresponding distances  $\rho_{0^\circ}, \rho_{30^\circ}, \rho_{45^\circ}, \rho_{90^\circ}, \rho_{135^\circ}, \rho_{150^\circ}$ , and  $\rho_{180^\circ}$  at which the given value of  $B$  is found. From Eq. (4b), a series of linear equations is obtained shown in Eq. (9). From Eq. (9), three sets of formulas for  $a$  and  $b$  can be obtained as shown in Eqs. (10)–(12). Each of these can be used to estimate a pair of ( $a, b$ ) from a given  $B$ . The shell parameters obtained in this way are generally less accurate than those obtained from the least squares method.

$$\begin{cases} \rho_{0^\circ} = a \cos(2 \times 0^\circ) + b = a + b & (9a) \\ \rho_{30^\circ} = a \cos(2 \times 30^\circ) + b = a/2 + b & (9b) \\ \rho_{45^\circ} = a \cos(2 \times 45^\circ) + b = b & (9c) \\ \rho_{90^\circ} = a \cos(2 \times 90^\circ) + b = -a + b & (9d) \\ \rho_{135^\circ} = a \cos(2 \times 135^\circ) + b = b & (9e) \\ \rho_{150^\circ} = a \cos(2 \times 150^\circ) + b = a/2 + b & (9f) \\ \rho_{180^\circ} = a \cos(2 \times 180^\circ) + b = a + b & (9g) \end{cases} \quad (9)$$

Because of inevitable measurement errors and slight variations in the magnetic field, the calculated  $a$  and  $b$  from Eqs. (10)–(12) may vary slightly. One way of handling these measurement variations and errors is to take an average of the values obtained from these three expressions.

$$\begin{bmatrix} a \\ b \end{bmatrix} = \begin{bmatrix} \frac{\rho_{0^\circ} + \rho_{180^\circ} - \rho_{45^\circ} - \rho_{135^\circ}}{2} \\ \frac{\rho_{45^\circ} + \rho_{135^\circ}}{2} \end{bmatrix} \quad (10)$$

$$\begin{bmatrix} a \\ b \end{bmatrix} = \begin{bmatrix} \rho_{0^\circ} + \rho_{180^\circ} - \rho_{30^\circ} - \rho_{150^\circ} \\ \rho_{30^\circ} + \rho_{150^\circ} - \frac{\rho_{0^\circ} + \rho_{180^\circ}}{2} \end{bmatrix} \quad (11)$$

$$\begin{bmatrix} a \\ b \end{bmatrix} = \begin{bmatrix} \frac{\rho_{0^\circ} + \rho_{180^\circ} - 2\rho_{90^\circ}}{4} \\ \frac{\rho_{0^\circ} + \rho_{180^\circ} + 2\rho_{90^\circ}}{4} \end{bmatrix} \quad (12)$$

This construction process should be repeated for each of the  $M$  data sets to define all of the shells.

### 6.3. Construction of the shell shape and size functions

Once  $M$  individual shells  $S(B_j, a_j, b_j)$ ,  $j = 1, 2, 3, \dots, M$ , are obtained, the constants,  $c_a, d_a, c_b,$  and  $d_b$ , in the shell shape function (4c) and the shell size function (4d) can be estimated by performing a regression fit with respect to  $B$ . A reasonably large number of shells ( $M \gg 1$ ) are needed to accurately estimate the values for these constants because these constants all vary nonlinearly with respect to  $B$ .

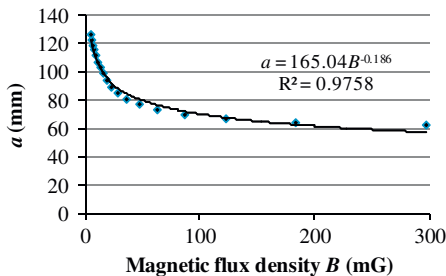


Fig. 13. Plot of a shell shape function  $a$ .

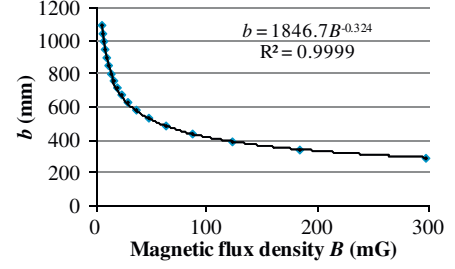


Fig. 14. Plot of a shell size function  $b$ .

Many regression methods can be used to obtain these constants. The expressions in Eq. (13) are those that produce optimum values with a total of  $M$  shells.

As an example of the regression accuracy, Figs. 13 and 14 show the shell shape function,  $a$ , and the shell size function,  $b$ , obtained in one experiment. A total of 18 shells were used to produce the functions shown in both figures.

$$\begin{cases} c_a = \exp \left( \frac{\sum_{j=1}^M \ln a_j \sum_{j=1}^M (\ln B_j)^2 - \sum_{j=1}^M (\ln B_j) \sum_{j=1}^M (\ln a_j \ln B_j)}{M \sum_{j=1}^M (\ln B_j)^2 - \left( \sum_{j=1}^M \ln B_j \right)^2} \right) \\ d_a = \frac{\sum_{j=1}^M \ln a_j \sum_{j=1}^M \ln B_j - M \sum_{j=1}^M (\ln a_j \ln B_j)}{M \sum_{j=1}^M (\ln B_j)^2 - \left( \sum_{j=1}^M \ln B_j \right)^2} \\ c_b = \exp \left( \frac{\sum_{j=1}^M \ln b_j \sum_{j=1}^M (\ln B_j)^2 - \sum_{j=1}^M (\ln B_j) \sum_{j=1}^M (\ln b_j \ln B_j)}{M \sum_{j=1}^M (\ln B_j)^2 - \left( \sum_{j=1}^M \ln B_j \right)^2} \right) \\ d_b = \frac{\sum_{j=1}^M \ln b_j \sum_{j=1}^M \ln B_j - M \sum_{j=1}^M (\ln b_j \ln B_j)}{M \sum_{j=1}^M (\ln B_j)^2 - \left( \sum_{j=1}^M \ln B_j \right)^2} \end{cases} \quad (13)$$

## 7. Anticipated application of the model

### 7.1. Locating a magnetic sensor at the intersection of two or more magnetic shells

One of the anticipated applications of the shell-based magnetic model is in a proximity detection system that uses measurements from two or more magnetic field generators to determine triangulated position of a sensor at the intersection point of the shells. This concept was tested with two generators on a 2-D coordinate system as shown in Fig. 15 on a large wooden platform. These two generators were positioned parallel to the  $x$ -axis and spaced 1.0 m apart. An example of two intersecting shells is given in the figure. These shells are modeled based on the constants shown in Figs. 13 and 14 with readings of 200 mG and 40 mG, respectively.

Using the measurements from the two alternately pulsed fields, the positions of 40 points on a triangular shaped path were determined. For these 40 points, the mean location error was 6.58 mm, the standard deviation of the error was 2.27 mm, and the maximum error was 11.67 mm compared to the actual location measurements. Fig. 16 shows the plots of both the actual and calculated locations.

### 7.2. Location determination of the magnetic sensor relative to the machine

The location of the magnetic sensor in the common coordinate system of the generators can, as shown in the previous section, be determined and continuously tracked as the intersection of the

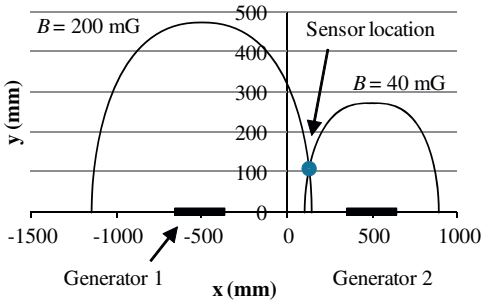


**Fig. 15.** Example sensor position determination using modeled shells of two generators with the constants,  $c_a = 165.04$ ,  $d_a = 0.186$ ,  $c_b = 1846.7$ , and  $d_b = 0.324$ , shown in Figs. 13 and 14.

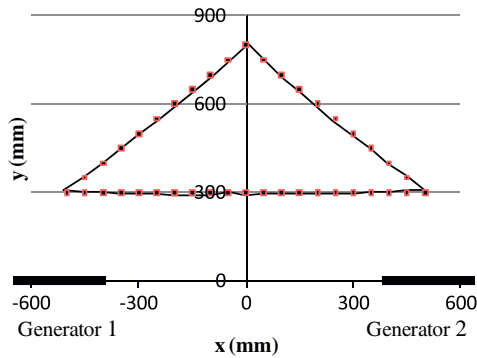


**Fig. 16.** Plots of both actual (dotted line) and calculated (solid line) locations over 40 points from a 2-D location application.

magnetic shells of the generators. The coordinate values of this location are mapped to the machine coordinate system. Based on the machine size and shape, the location of the sensor relative to specific parts of the machine can then be determined. Based on the sensor location and the state of the machine, the proximity detection control system can take the necessary action to protect the worker by preventing any potentially hazardous machine motion.

### 7.3. Discussion on locating accuracy with the model

A close inspection of Fig. 16 shows that all 40 calculated positions have a relatively uniform accuracy in the space both near to and far from the generators. The uniformly distributed accuracy of these calculated positions is attributed, in part, to the uniform accuracy of the shell-based model over its defined space. In cases when it is difficult to obtain the calculated locations within an acceptable accuracy over a required space by approximating the shells with other geometric shapes such as spheres or ellipsoids this shell-based model may provide better results.

The exercise of locating a magnetic sensor at the intersection of two magnetic shells was considered a comprehensive laboratory test of the shell-based model and the locating methodology for a potential advanced technology for magnetic proximity detection systems.

## 8. Current and future work

A prototype intelligent proximity detection system has been installed and tested on a JOY CMM at the NIOSH laboratory in Pittsburgh (Carr et al., 2010). This prototype system is built around

commercially available hardware including four ferrite-cored generators and wearable sensors. The data from the proximity hardware is used in the prototype system by an onboard controller, which performs the triangulation calculations and sends output controls to a bank of relays to interdict individual machine motions. Using this prototype system, experiments have been conducted in which a wearable magnetic sensor was successfully located at an intersection of two or more shells in 3-D space around the machine. However, the test also revealed some issues which could be addressed in the future research and development of this technology. One of these issues was that the magnetic field distribution changes when the generators are positioned very close to metal parts of the machine resulting in changes of shell shape and size. The changes varied with the shapes and sizes as well as types of the metal. These effects were minimized by performing the model construction procedure with the generators mounted in place on the machine. However, developing a more basic understanding of the impact that metal masses have on ferrite-cored generators and incorporating these findings into the basic shell-based model introduced in this paper is expected to bring forth more sophisticated models with improved accuracy.

NIOSH research with the prototype intelligent proximity detection system is continuing. This research is currently focused on incorporating measurement of worker posture, incorporating a visual warning system, and quantifying the expected safety gain to be achieved with the implementation of this technology.

## 9. Summary

A detailed discussion of the basic empirical shell-based magnetic flux density distribution model for ferrite-cored magnetic generators used in some proximity detection systems is presented. The evaluations show that the model retains uniform accuracy in its defined space around a generator in a medium of uniform permeability. The model lays the groundwork for an advanced proximity detection system that can accurately locate workers using triangulation. A systematic construction process of the model for individual generators using field measurement data is also presented. The laboratory data acquisition scheme is presented as well and can be generalized and adapted for various working environments for field data acquisition. As demonstrated in the paper, the exact location of a worker carrying a magnetic sensor can be determined at the intersection of multiple shells generated from their field distribution models of multiple generators in a proximity detection system. The goal is to know the exact location of a worker near a mobile machine so the worker can be more effectively protected from being struck or pinned by the machine. More generally, the model can be used for near-field distribution studies of ferrite-cored magnetic field radiators.

## Disclaimer

The findings and conclusions in this report are those of the authors and do not necessarily represent the views of the National Institute for Occupational Safety and Health.

## Acknowledgements

The authors wish to thank Joseph DuCarme, Timothy Matty, Justin Srednicki, Justin Patts and Amber Jobses at the NIOSH Pittsburgh location for their help and suggestions during the course of this work. The authors wish to thank Dr. Joseph A. Waynert and Mr. Todd M. Ruff for their comments and suggestions during the review of this paper.

## References

- Bartels et al., 2005. Continuous mining: a pilot study of the role of visual attention locations and work position in underground coal mines. *Professional Safety* 1, 28–35.
- Bartels et al., 2008. Analyzing factors influencing struck-by accidents of a moving mining machine by using motion capture and DHM simulations. In: *Digital Human Modeling for Design and Engineering Conference and Exhibition*, June 17–19, 2008, Pittsburgh, PA, USA.
- Buchsbaum, L., 2011. Ready or not, MSHA believes proximity detection can save lives. *Coal Age* 116 (2), 36–38.
- Carr et al., 2010. Development of a method to determine operator location using electromagnetic proximity detection. In: *International Workshop on Robotic Sensors Environments*, October 15–16, 2010, Phoenix, AZ, USA.
- Chirdon, 2009. MSHA Proximity Detection. <[http://www.msha.gov/Accident\\_Prevention/NewTechnologies/ProximityDetection/Proximity%20Detection%20Paper.pdf](http://www.msha.gov/Accident_Prevention/NewTechnologies/ProximityDetection/Proximity%20Detection%20Paper.pdf)>.
- Dransite et al., 2011. Remote Controlled Continuous Mining Machine Fatal Analysis Report of Victim's Physical Location with Respect to the Machine. Original report dated April 26, 2002. <<http://www.msha.gov/webcasts/Coal2005/Fatal%20Accident%20Summary.pdf>> (updated 31.03.11).
- Li et al., 2010. Modeling of the magnetic field around a ferrite-cored generator in a proximity detection system. In: *14th Conference on Electromagnetic Field Computation*, May 9–12, 2010, Chicago, IL, USA.
- Ruff, 2010. Overview of Proximity Warning and Technologies and Approaches, presentation at NIOSH Workshop on Proximity Warning Systems for Mining Equipment, Charleston, WV, September 15, 2010. <[http://www.cdc.gov/niosh/mining/workshops/machinesafety/workshop2010/Ruff-NIOSH-PDWorkshop\\_2010-508.pdf](http://www.cdc.gov/niosh/mining/workshops/machinesafety/workshop2010/Ruff-NIOSH-PDWorkshop_2010-508.pdf)>.
- Schiffbauer, 2002. Active proximity warning system for surface and underground mining applications. *Mining Engineering* (December 01).